Optical properties of bimodally distributed InAs quantum dots grown on digital AlAs$_{0.56}$Sb$_{0.44}$ matrix for use in intermediate band solar cells

Mukul C. Debnath, Baolai Liang, Ramesh B. Laghumavarapu, Guodong Wang, Aparna Das, Bor-Chau Juang, and Diana L. Huffaker

Articles you may be interested in

Electronic and optical properties of Cu$_2$XSnS$_4$ (X = Be, Mg, Ca, Mn, Fe, and Ni) and the impact of native defect pairs
Journal of Applied Physics **121**, 203104 (2017); 10.1063/1.4984115

Hierarchical structures of magnetic nanoparticles for controlling magnetic interactions on three different length scales
Journal of Applied Physics **121**, 224303 (2017); 10.1063/1.4983849

Noncollinear antiferromagnetic Haldane magnon insulator
Journal of Applied Physics **121**, 223904 (2017); 10.1063/1.4985615

Focused beams of fast neutral atoms in glow discharge plasma
Journal of Applied Physics **121**, 223302 (2017); 10.1063/1.4985249

Single-crystal N-polar GaN p-n diodes by plasma-assisted molecular beam epitaxy
Applied Physics Letters **110**, 253506 (2017); 10.1063/1.4989581

Two-step photocurrent generation enhanced by miniband formation in InAs/GaAs quantum dot superlattice intermediate-band solar cells
Applied Physics Letters **110**, 193104 (2017); 10.1063/1.4983288

Optical properties of bimodally distributed InAs quantum dots grown on digital AlAs$_{0.56}$Sb$_{0.44}$ matrix for use in intermediate band solar cells

Mukul C. Debnath,[a)] Baolai Liang, Ramesh B. Laghumavarapu, Guodong Wang, Aparna Das, Bor-Chau Juang, and Diana L. Huffaker
California NanoSystems Institute and Department of Electrical Engineering, University of California-Los Angeles, Los Angeles, California 90095, USA

High-quality InAs quantum dots (QDs) with nominal thicknesses of 5.0–8.0 monolayers were grown on a digital AlAs$_{0.56}$Sb$_{0.44}$ matrix lattice-matched to the InP(001) substrate. All QDs showed bimodal size distribution, and their optical properties were investigated by photoluminescence (PL) and time-resolved PL measurements. Power dependent PL exhibited a linear relationship between the peak energy and the cube root of the excitation power for both the small QD family (SQDF) and the large QD family (LQDF), which is attributed to the type-II transition. The PL intensity, peak energy, and carrier lifetime of SQDF and LQDF showed very sensitive at high temperature. Above 125 K, the PL intensity ratio increased continuously between LQDF and SQDF, the peak energy shifted anomalously in SQDF, and the longer carrier radiative lifetime (≥ 3.0 ns at 77 K) reduced rapidly in SQDF and slowly in LQDF. These results are ascribed to thermally activated carrier escape from SQDF into the wetting layer, which then relaxed into LQDF with low-localized energy states. *Published by AIP Publishing.* [http://dx.doi.org/10.1063/1.4984832]

I. INTRODUCTION

Intermediate band solar cells (IBSCs), proposed by Luque and Martí,[1] are promising candidates for high-efficiency single junction solar cells. Theoretically, it is predicted that IBSCs could exceed the Shockley-Queisser limit[2] and achieve efficiencies more than 60%, much higher than multijunction solar cell efficiencies of ∼40%.[3] However, establishing an IB energy level between the conduction band (CB) and valence band (VB) of the host material is challenging. An IB material within a wide bandgap host material is needed for sequential absorption of photons with multiple energies among VB, IB, and CB. One possible route to form IB is from highly uniform closely spaced quantum dots (QDs), where a miniband is formed by a strong wave function overlapping between QDs. In an ideal IBSC, intermediate transitions of 0.7 eV (VB to IB) and 1.23 eV (IB to CB) are needed in a 1.92 eV of the host material bandgap.[4]

To realize such an IB and IBSCs, several types of QD material systems, e.g., InAs/GaAs,[5,6] InGaAs/GaAs,[7] GaSb/InGaAs,[8] and InAs/GaAsSb[9,10] QDs, were studied. Unfortunately, none of them has fulfilled those ideal intermediate transitions for IBSCs. InAs QDs with AlAs$_{0.56}$Sb$_{0.44}$ matrix layers are one of the most promising candidates for IBSCs. Bandgaps of ∼0.7 and ∼1.92 eV are available for QDs and matrix layers, respectively. Matrix layer AlAs$_{0.56}$Sb$_{0.44}$ (hereafter referred to as AlAsSb) can be grown lattice-matched to the InP substrate. The indirect bandgap of the host material AlAsSb (1.89 eV) is very close to the optimal IBSC bandgap of 1.92 eV, while the direct bandgap is around 2.56 eV.[11] Moreover, InAs forms a type-II band alignment with AlAsSb, with a very small (or zero) VB offset and a large CB offset, making the combination of these two materials favorable for IBSCs. The type-II band alignment leads to longer carrier lifetime in the QD states, which is also beneficial for the efficiency of IBSCs.[10,12,13]

Due to the wide miscibility bandgap, growth of high-quality and lattice-matched AlAsSb is extremely challenging because of the non-unity sticking coefficient of group-V species with a high incorporation coefficient of As$_2$ relative to that of Sb$_2$.[14] For conventional molecular beam epitaxy (MBE) growth of random or analog AlAsSb alloys, both fast fluctuations and slow drifts in group-V cell temperatures can result in composition fluctuations. Even small fluctuations from the exact lattice-matched condition can cause strain relaxation, resulting in the formation of the defects of dislocations. In order to get the precise lattice-matched condition, digitally grown AlAsSb takes advantages of the control of the shutters to obtain the desired alloy composition with high crystalline quality.[15] Previously, we reported the growth of InAs QDs with an analog AlAsSb matrix and GaAsSb/GaAs cladding layers.[16] We noticed that the analog growth method leads to fluctuations in the AlAsSb composition within a single sample and sample to sample. So, we developed InAs QDs directly on a digital AlAsSb matrix for the easier alloy composition control. In this paper, we report the growth of InAs QDs on a digital AlAsSb matrix by MBE for the first time and present their optical properties by steady-state [power- and temperature-dependent] photoluminescence (PL) and time-resolved PL (TRPL) measurements.

II. GROWTH OF InAs/AlAsSb QDs AND EXPERIMENTAL SET-UP

InAs/AlAsSb QD structures were grown on epi-ready semi-insulating InP(001) substrate by using Veeco GEN930 solid-source MBE system. In this system, both As$_2$ and Sb$_2$

a)Author to whom correspondence should be addressed: mdebnath@cnsi.ucla.edu

fluxes are supplied using valved cracker cells with cracker temperatures at 900 °C. The growth procedures for InAs/ AlAsSb QD structures are critical for obtaining a high-quality lattice-matched AlAsSb matrix layer and a high-density QD layer on it. Figure 1(a) shows the schematic of the stacked QD structure [capped and uncapped InAs QDs with the digital AlAsSb matrix] (left) and InAs/ $AlAs_{0.56}Sb_{0.44}$ QD band structure (right) grown for this study. Oxide desorption and growth were monitored by *in situ* reflection high-energy electron diffraction (RHEED). After oxide desorption of the InP substrate at $\sim$530 °C with As_2 flux, a digital alloy 200-nm thick AlAsSb buffer layer was grown at a substrate temperature (T_{sub}) of $\sim$500 °C. During the digital alloy growth, the Al shutter was kept open all the time, while As and Sb shutters were alternately opened and closed. In order to get the lattice-matched
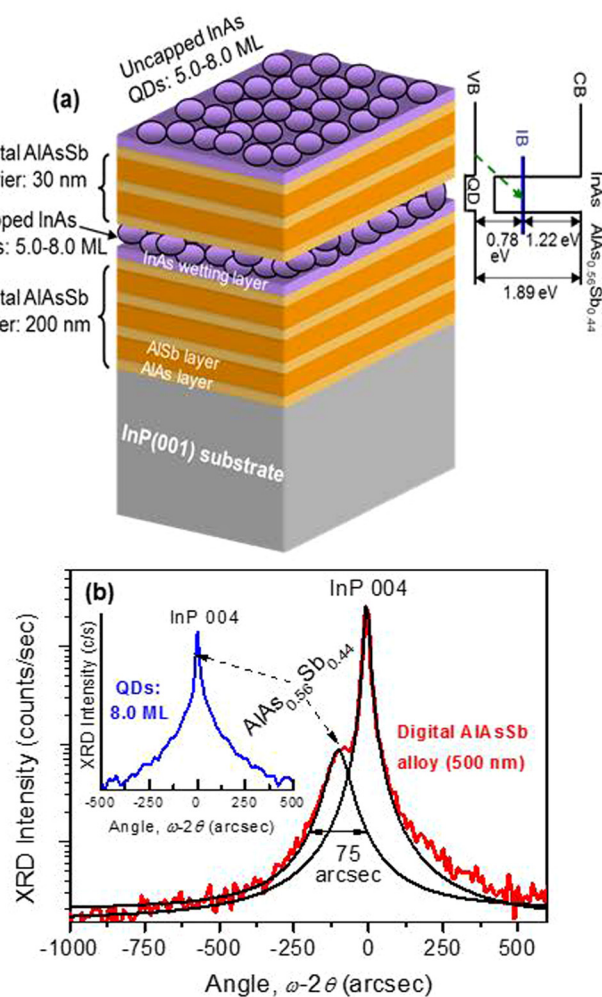

FIG. 1. (a) Schematic stacked structure of the capped and uncapped InAs QDs with the digital $AlAs_{1-x}Sb_x$ matrix (left) and the InAs/AlAs$_{0.56}$Sb$_{0.44}$ QDs band structure (right). Digital $AlAs_{1-x}Sb_x$ alloy was grown by a short period of superlattice with alternating layers of AlAs and AlSb. The dotted arrow in the QD band structure represents the carrier transition from the VB to the IB. All eV values in the band structure are taken from Ref. 11. (b) XRD ω-2θ scan around the 004 reflections of 500-nm thick digital AlAs$_{0.56}$Sb$_{0.44}$ alloy grown on the InP substrate. XRD data (red lines) are fitted with Gaussian function (black lines) from which the linewidth of AlAs$_{0.56}$Sb$_{0.44}$ layer is determined. The inset also shows the XRD ω-2θ scan of the AlAs$_{0.56}$Sb$_{0.44}$ 004 reflections due to the matrix layer in a 8.0 ML QD structure grown on InP(001) substrates.

condition of the digital AlAsSb alloy, a short period superlattice ($\sim$13 Å period) was grown with rapidly alternating layers of AlAs (1.7 Å) and AlSb (11.4 Å) [see the schematic in Fig. 1(a)], provided a reproducible alloy using an As_2/Sb_2 beam equivalent pressure (BEP) ratio of $\sim$6 [e.g., As_2 BEP $\sim$4.5 $\times 10^{-6}$ Torr and Sb_2 BEP $\sim$7.5 $\times 10^{-7}$ Torr], Al growth rate = 0.44 monolayer (ML)/s [Al BEP $\sim$6.5 $\times 10^{-8}$ Torr], and As-shutter duty cycle (As-SDC) $\approx$ 0.14. The average AlAs mole fraction of x in the $AlAs_xSb_{1-x}$ alloy was controlled by this As-SDC = (As shutter time)/(As shutter time + Sb shutter time).[15]

After completing a thick digital AlAsSb buffer layer, InAs QD growth on a top AlAs surface was initiated by the conventional MBE method using T_{sub} = 500 °C and a growth rate of 0.08 ML/s under an As_2/In BEP ratio $\sim$55. With a deposition of $\sim$4.90 ML of InAs, which formed as a two-dimensional wetting layer (WL) on the AlAsSb buffer layer, the RHEED pattern quickly transforms from streaky (1 × 3) to spotty AlAsSb, indicating a three-dimensional growth. Self-assembled InAs QDs were spontaneously formed through the Stranski-Krastanov growth mode. We found that the critical thickness of InAs QDs on AlAsSb buffer was $\sim$4.9 ML for which RHEED exhibited a chevron type pattern of QD formation. For this study, we grew a set of single layer InAs QDs with a nominal deposition thickness of 5.0–8.0 ML. For PL measurements, QDs were capped with a 30-nm thick digital AlAsSb barrier under the same growth conditions used for the buffer layer. On the top surface, an uncapped InAs QD layer was grown for *ex-situ* atomic force microscopy (AFM) analysis. The capped QD layers were annealed under an As_2 flux by maintaining the T_{sub} for 30–40 s, while the uncapped QD layer was rapidly cooled to room temperature. It is assumed that the morphology of the uncapped and capped QDs is similar under the same growth condition. However, the actual morphology of capped and uncapped QDs may be varied during annealing and rapid cooling of QDs within the same growth run. Also, the deposition of a capping layer may suppress the coalescence of the dots, which could affect the morphology of the QDs such as size, shape, density, and composition. It is also known that a thin capping layer provided partial relaxation of the elastic strain in the QDs.[17] A detailed study of the morphology of capped and uncapped InAs/GaAs QDs and their electrical-optical properties was described in the literature.[17]

It should be mentioned that before growing QD samples, the lattice-matched condition of AlAsSb was determined from a set of 300–500-nm thick digital alloys grown with different As_2/Sb_2 BEP ratios between 2.0 and 10.0 and As-SDC between 0.1 and 0.2. An optimized lattice-matched digital AlAsSb alloy was obtained with an As_2/Sb_2 BEP ratio of 6.20 and As-SDC of 0.138. The x-ray diffraction (XRD) of the ω-2θ scan of such a lattice-matched digital AlAsSb alloy (500-nm thick) provided the narrowest linewidth of 75 arc sec, as shown from Gaussian fitting (black lines) with experimental data (red lines) in Fig. 1(b). On the other hand, an analog AlAsSb layer (same thickness, 500-nm) provided a higher XRD linewidth of $\sim$100 arc sec (not shown here). XRD data also showed that the digital AlAsSb matrix used for the growth

of all QDs (5.0–8.0 ML) is well lattice-matched with the InP substrate, as shown for a 8.0 ML QD in the inset of Fig. 1(b). XRD results indicate that the digital AlAsSb alloy was formed with a good crystalline quality with reliable composition control.

The surface morphology and the dot size of uncapped InAs QDs were evaluated using a Bruker AFM in a tapping mode. To analyze the optical properties of the QDs, temperature and power dependent PL measurements were carried out between 77 and 300 K using a 532 nm (2.33 eV) pump laser with a maximum excitation power density of $\sim$200 mW/cm^2. PL emission after monochromator dispersion is measured using an extended InGaAs detector with a cut-off wavelength at 2560 nm (0.48 eV). The TRPL measurements were carried out using a Super-continuum pulse laser [$\lambda = 650$ nm (1.91 eV)] and a time-correlated single photon counting system (TCSPC PicoHarp 300) to record the decay traces from the QDs.

III. RESULTS AND DISCUSSION

A. Evaluation of QD size and density by AFM

For this study, all QDs were grown under the same growth conditions. Immediately after growth, density and size distribution of all QDs were derived from in-air AFM measurements. Figure 2(a) shows the AFM image $(1.0 \times 1.0 \, \mu m^2$ scanned area) taken from an uncapped 8.0 ML InAs QD. Figure 2(b)
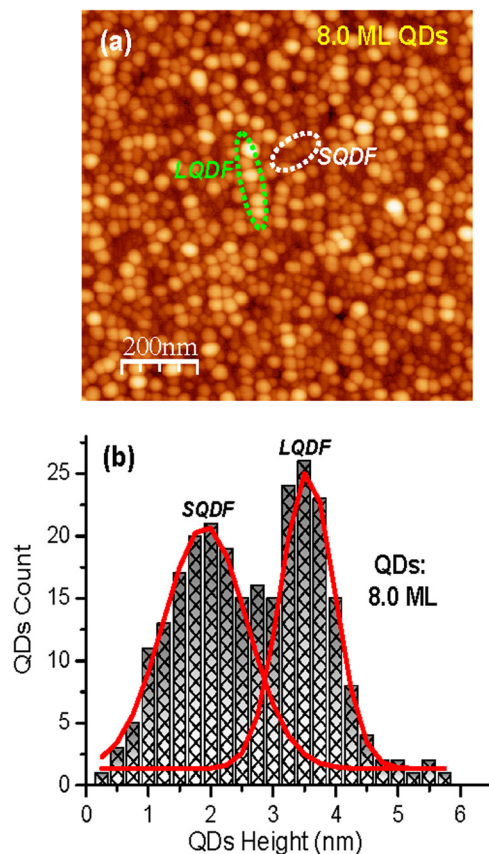
FIG. 2. (a) AFM image $(1.0 \times 1.0 \, \mu m^2$ scanned area) from the uncapped InAs QD layer with a nominal 8.0 ML thickness. The representative QD family of SQDF and LQDF is shown by the dotted area in the image. (b) The size histogram with height distributions is fitted by the two-Gaussian distribution function.

shows the size histogram with the height distribution measured from the 500×500 nm^2 area of the same AFM image. It is evident from the AFM image that this sample showed two different QD families, namely, the small QD family (SQDF) and large QD family (LQDF), as shown by the dotted area in the image. All other QD samples (5.0–7.0 ML) also showed similar two QD families of SQDF and LQDF. The size histogram in Fig. 2(b) is fitted by two-Gaussian line shapes with two peaks of SQDF and LQDF and can be attributed to the bimodal QD size distribution.[18–20] The average height/diameter of SQDF and LQDF in the 8.0 ML QD sample is (2.0 ± 0.5) nm/(25.0 ± 2.8) nm and (3.85 ± 0.8) nm/(40.0 ± 3.0) nm, respectively. AFM images also show that 8.0 ML QDs are more closely contacted among dots compared to those of other lower thicknesses QDs (e.g., 5.0 ML), indicating higher dot density. The average areal density of SQDF and LQDF is $\sim$3.5 $\times 10^{10}$/cm^2 and $\sim$5.5 $\times 10^{10}$/cm^2, respectively, in 8.0 ML QDs (total density $\sim$9.0 $\times 10^{10}$/cm^2), which is higher than that of lower thickness 5.0 ML QDs (total density $\sim$5.0 $\times 10^{10}$/cm^2, not shown here). We found that the dot densities in LQDF are slightly higher than those in SQDF. We also found that the average size and areal density of both SQDF and LQDF were increased with increasing InAs deposition thickness. Similar results were also obtained in bimodal InAs/GaAs QDs,[21] and this behavior has been explained in terms of the interaction between dots and the barrier around the dot edges.[22,23] It should be noted that the behavior of bimodal QD size distributions is not only from the difference in the size of the deposition layers but also from the intrinsic properties of each layer, which will be discussed in detail in Secs. III B–III D.

B. Bimodally distributed QDs measured by 77 K PL

Figure 3 shows 77 K normalized PL spectra of InAs QDs with thicknesses of 5.0 ML (violet line), 6.0 ML (blue line), 7.0 ML (green line), and 8.0 ML (red line) measured at 15 mW/cm^2 of excitation power density. Figure 3 also shows a 4.0 ML InAs WL sample (black line) with a peak indicated at 930 nm and an associated InP substrate peak at 905 nm. The red shift in the peak emission wavelength (energy scale also shown in the top x-axis) with the increase in the InAs deposition thickness reflects the growth of the QD size.[24] Also, the red shift in the PL emission could be partially explained by increased strain relief in InAs QDs.[10,25] All QD PL spectra show doublet-like feature and could be well fitted using two-Gaussian line shapes, as shown by the dotted lines and the shaded area (e.g., 8.0 ML QDs). In bimodal QDs, the exciton localized in the SQDF contributes to the higher energy peak (indicated by an arrow with SQDF) and LQDF contributes to the lower energy peak (also indicated by an arrow with LQDF), according to the quantum-size effect. Since the QD density of LQDF is higher, the PL intensity of LQDF is stronger than that of SQDF. The absence (or very weak) of the PL signal from the AlAsSb matrix (InAs WL) in the QDs suggests that the carriers are efficiently captured by SQDF and LQDF before they can recombine within the WL and/or matrix. We found that the PL intensity increases with increasing nominal deposition thickness. The overall
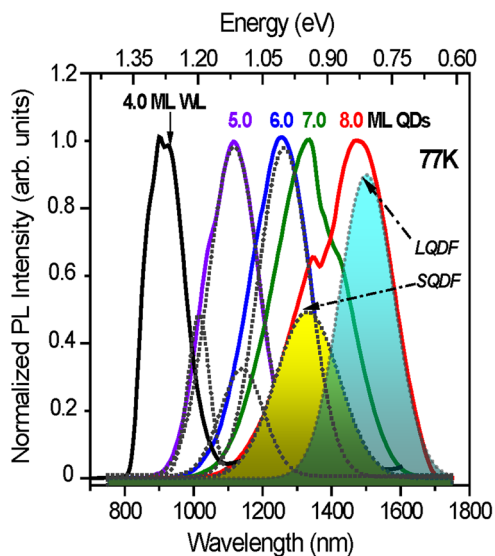
FIG. 3. Normalized 77 K PL spectra of InAs QDs with thicknesses of 5.0 ML (violet line), 6.0 ML (blue line), 7.0 ML (green line), and 8.0 ML (red line) including a 4.0 ML InAs wetting layer sample (black line). PL spectra are fitted with two-Gaussian line shapes as shown by dotted lines and shaded area (e.g., 8.0 ML QDs with peaks of SQDF and LQDF).

integrated PL intensity of SQDF and LQDF in 8.0 ML QDs is ~2 times higher than that in 5.0 ML QDs. The full width at half maximum (FWHM) of the deconvoluted spectra of SQDF varies from 50 to 120 meV, whereas that of LQDF slightly decreases from 85 to 81 meV with an increasing deposition thickness from 5.0 to 8.0 ML. The energy separation of the two peaks of SQDF and LQDF is ~70 meV, which depends linearly on the excitation power density over five orders of magnitude [see Fig. 4(a)]. The fact that these two peaks also can be seen at very low excitation power density of 0.05 mW/cm^2 (will be described in Sec. III C) suggests that they correspond to the ground state transition from two QD families and excluded any transition from excited states of QDs or InAs WL.

C. Excitation power dependent PL

Since all QDs presented here are bimodal and show almost similar characteristics, we will focus only on the 8.0 ML QD sample for power- and temperature-dependent PL analysis. In order to verify the origin of the double peak feature and the carrier confinement in the QD structures, power-dependent PL experiments were performed at 77 K. Figure 4(a) shows three different power-dependent PL spectra measured from 0.05 to 15 mW/cm^2. At the lowest excitation power density of 0.05 mW/cm^2, broader and asymmetric PL spectra (shown by magnified green curve) are fitted with two-Gaussian line shapes (shown by dotted lines), which evolve from SQDF and LQDF. The shapes of the PL spectra did not change significantly with increasing excitation power density. The overall PL intensities of SQDF and LQDF are enhanced almost linearly. The intensity of the low energy peak of LQDF remains stronger than that of the higher energy peak of SQDF, and their relative intensity is nearly the same over the entire excitation power density measured from 0.05 to 15 mW/cm^2. These results clearly indicate
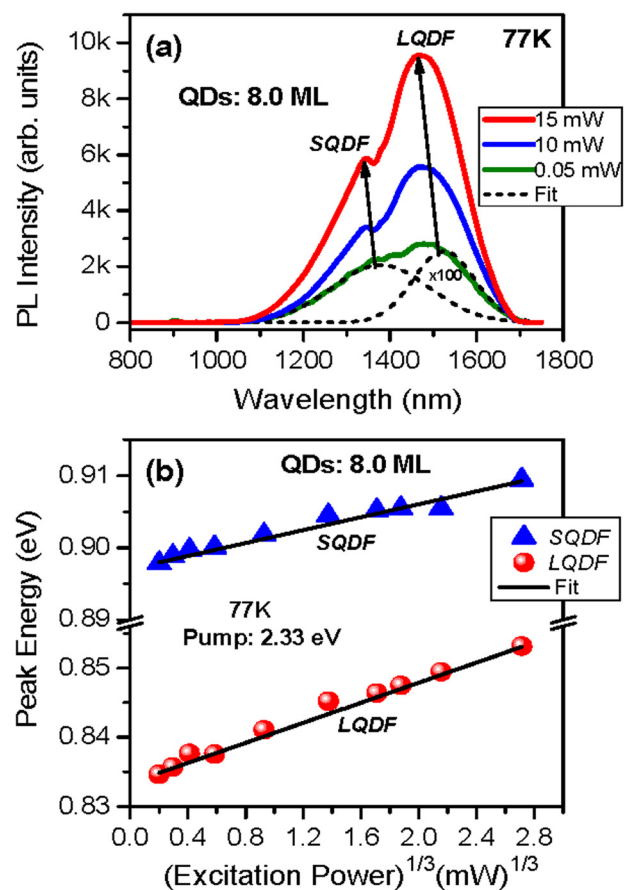

FIG. 4. (a) Power-dependent 77 K PL spectra from the 8.0 ML QD structure. Broader PL spectra were fitted with two-Gaussian line shapes as shown them by dotted lines for the lowest excitation power density of 0.05 mW/cm^2. (b) PL peak position is shown for SQDF [(blue) triangles] and LQDF [(red) circles] in 8.0 ML QDs as a function of the cube root of the excitation power.

that two peaks of SQDF and LQDF are attributed to the bimodal size distribution of the QDs. The peak positions of both SQDF and LQDF shift to higher energy with increasing excitation power, as indicated by arrows in Fig. 4(a). We noticed that the blue shift in LQDF is larger (18.5 meV) than in SQDF (11.6 meV). The rate of blue-shift in LQDF and SQDF may be accompanied by a change in the spatial distribution of the electron and hole wave function between the InAs QDs and the AlAsSb matrix. It is known that a type-II structure enables the energy bending effect with increasing excitation power and induces those blue shifts in the PL.[26]

Figure 4(b) shows the cube root power dependence of the peak energy of SQDF [(blue) triangles] and LQDF [(red) circles] in 8.0 ML QDs. It is well known that the position of the PL peak energy should be independent of excitation power for a type-I transition, while a linear relationship between the PL peak energy and the cube root of the excitation power is a signature of a type-II transition.[27] A cube root relationship is explained by an equation: $E_{peak} \propto I_{exc}^{1/3}$, where E_{peak} is the PL peak energy and I_{exc} is the excitation power density. The power-dependent PL with 8.0 ML QDs (both SQDF and LQDF) clearly exhibited this signature of a type-II transition because the selection rule is absent due to the spatial separation of electrons and holes between the InAs QDs and the AlAsSb matrix.

In a type-II transition, nonequilibrium carriers of electrons are captured by the InAs QDs that locally bend the conduction band edge, while holes are localized in the AlAsSb matrix due to Coulomb attraction to the electrons. After optical pumping, the rearrangement of the nonequilibrium carrier density induced by the band-bending effect modifies the optical transition probability. Since nonequilibrium carriers continuously recombine during the radiative recombination process, the band-bending effect decreases. As a result, the overlap between electron and hole wave functions is reduced in the matrix layer, leading to a longer radiative lifetime.[28,29] In contrast, for a type-I transition, the electron wave function penetrates more into the matrix layer and the overlap between the electron and hole wave functions increases, which leads to a faster decay time (i.e., shorter carrier lifetime). In Sec. III E, the power- and temperature-dependence carrier lifetime of our bimodal InAs/AlAsSb QDs will be discussed.

D. Temperature dependent PL

Temperature dependent PL was measured to investigate the QD bimodal size distribution and thermally activated carrier transfer process of different dot families. Figure 5(a)
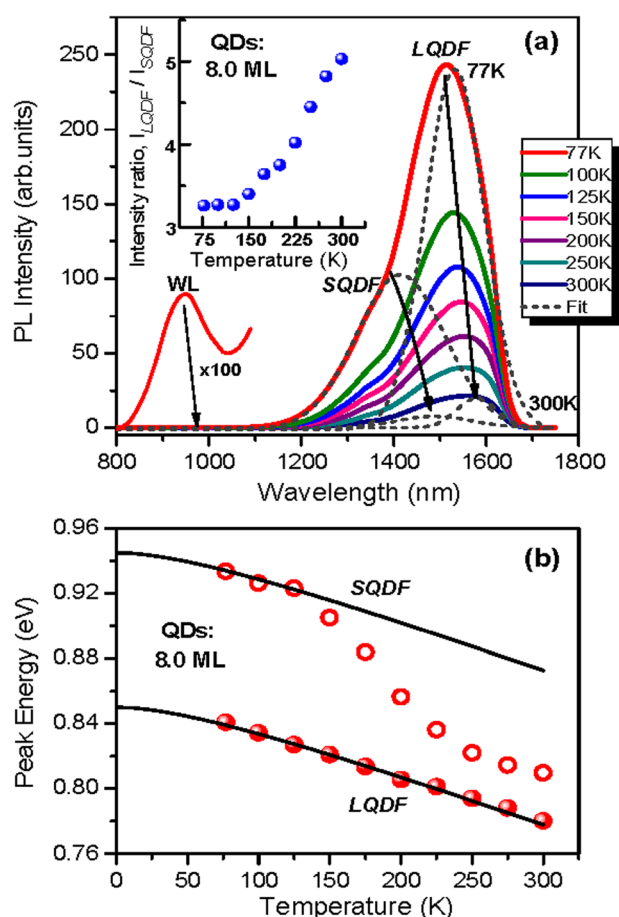

FIG. 5. (a) Temperature-dependent PL spectra of 8.0 ML QDs at a low excitation power density of 1 mW/cm². A magnified 77 K WL peak is shown at ~930 nm. The inset shows the PL intensity ratio between LQDF and SQDF as a function of temperature in 8.0 ML QDs. (b) The temperature dependence of the PL peak energies of SQDF (open circles) and LQDF (filled circles) in 8.0 ML QDs is fitted (solid lines) by the Varshni law.

shows the temperature dependent PL spectra of 8.0 ML QDs measured from 77 to 300 K at 1 mW/cm². PL spectra also show very weak WL emission at lower wavelength side. A magnified 77 K WL peak is shown at ~930 nm, which is identical to a 4.0 ML InAs WL peak position shown in Fig. 3. A very weak WL emission indicated that no any extra carrier injection took place from WL into SQDF or LQDF, but it may work as an activated carrier channel at elevated temperature.[30] As shown here, PL thermal quenching starts at relatively low temperature ~100 K, which is a characteristic of type-II QDs. Temperature dependent PL spectra also show a broader and asymmetric line shape as seen in power dependent PL spectra [Fig. 4(a)], and it could be deconvoluted into two Gaussian peaks of SQDF and LQDF, as shown by fitted dotted lines at 77 K and 300 K. With increasing temperature, PL peaks of SQDF and LQDF show a typical red shift due to the thermal expansion of the lattice constant and decrease of the QD bandgap. The relative PL intensity of LQDF and SQDF is almost the same up to 125 K, while the PL intensity is dominant by LQDF emission above 125 K. The inset of Fig. 5(a) shows the PL intensity ratio of LQDF and SQDF as a function of temperature in 8.0 ML QDs. The almost constant PL intensity ratio within 77–125 K indicates the absence of carrier escape between dot families. However, with increasing temperature above 125 K, the continuous increase in the PL intensity ratio indicates that carriers are thermally activated from SQDF into the WL and then relax into LQDF with relatively low-localized energy states. A similar carrier escape process was also reported in the bimodal InAs/GaAs and InGaAs/GaAs QD system,[18,31,32] and a quantitative model analysis in which the carrier transfer between SQDF and LQDF was facilitated by the WL state in InAs/GaAs QDs system was also reported.[33]

Figure 5(b) shows the temperature dependence of the PL peak energy in 8.0 ML QDs. The peak energies of SQDF (open circles) and LQDF (filled circles) are fitted by the Varshni law[34] expressed as $E_g(T) = E_g(0) - \alpha T^2/(\beta + T)$ with parameters $\alpha = 3.16 \times 10^{-4}$ eV/K and $\beta = 93$ K used for bulk InAs. The peak energy of LQDF nicely follows the Varshni law as shown by fitted line over the whole measured temperature range, while an anomalous energy shift has been found for SQDF. Above 125 K, the peak energy of SQDF did not follow the functional form of the Varshni law, as the experimental points are deviated from the fitted line. A strong PL thermal quenching at high temperature with an activation energy in the order of ~70 meV (obtained from the Arrhenius plot of PL integrated intensity vs 1000/T, not shown here) and the anomalous energy shift above 125 K indicate a typical temperature dependence of bimodal QD behavior[18] and also confirm the carrier redistribution between two different sizes of QDs families through the WL as a carrier transfer channel.[20]

It is important to note that at room temperature, LQDF in 8.0 ML QD peak energy is ~0.78 eV [see Fig. 5(b)], which is close to the optimal value of 0.7 eV for an ideal IBSC.[1,4] The IBSC theory predicts that only when the band alignment is close to the optimal value, the maximum power conversion efficiency could be achieved. We found that a 9.0 ML QD (LQDF) has room temperature PL peak energy

at 0.75 eV, which is even more close to that optimal value for an ideal IBSC. We speculate that a careful InAs/AlAsSb QD design with a further increase in the nominal deposition thickness >9.0 ML could approach to that exact optimal transition, as needed for highly efficient IBSCs.

E. Carrier lifetime and carrier transfer determined by TRPL

A variety of thermally activated carrier escape and transfer processes have been investigated in InAs/GaAs,[30,35] InAs/InGaAs,[36] InAs/InP,[37] and InP/AlGaInP[38] QD systems by TRPL measurements. We also performed TRPL measurements to determine the carrier lifetimes as well as to understand the carrier transfer process in more detail in our bimodal InAs/AlAsSb QD structures. Figure 6(a) shows 77 K PL decay curves of the 8.0 ML QD structure with different detection wavelengths from 1600 to 1345 nm, including two detected peak wavelengths for LQDF (1515 nm, blue curve) and SQDF (1345 nm, purple curve) measured at 1.0 mW/cm^2. All PL decay curves are well fitted by the double-exponential decay function with fast and slow decay time constants, as shown them by solid black lines. We found that the fast decay time constant is almost the same ~0.70 ns, while the slow decay time constant varies from 3.65 to 2.75 ns with wavelengths of 1600–1345 nm. The fast decay

FIG. 6. (a) 77 K PL decay curves of the 8.0 ML QD structure at different detection wavelengths from 1600 nm to 1345 nm measured at 1 mW/cm^2. (b) Carrier lifetime of 8.0 ML QDs as a function of detection wavelength. The solid line connecting the data points is a guide to the eye.

time constant (~0.70 ns) could be explained by the competition between optical recombination from carriers confined inside QDs (here SQDF or LQDF) and the rapid carrier transfer to the WL and/or matrix layer. The slow decay time constant ($\geq$3.0 ns) is assigned to the carrier lifetime (τ) that confined inside the quantum states of the SQDF or LQDF. Also, this slow decay time constant, i.e., longer carrier lifetime, could be attributed to type-II transition. A similar longer carrier lifetime related to type-II transitions is reported in GaSb/GaAs,[39,40] InAs/GaAsSb,[10,13,29] and InAs/GaAsSb/AlAsSb[41] QD systems.

Figure 6(b) shows τ as a function of detection wavelength. It shows that τ decreases from 3.65 ns to 2.75 ns with decreasing detected wavelength from 1600 nm to 1345 nm, respectively. The value of τ obtained was 3.37 ns for LQDF (1515 nm) and 2.75 ns for SQDF (1345 nm). We found that all these values of τ are almost the same with increasing excitation power up to 15 mW/cm^2, indicating that radiative lifetime of the bimodal InAs/AlAsSb QD structure is power independent. It is known that decreasing detection wavelength probe in the QD ensemble, the PL emission evolves from small QDs and the carrier lifetime becomes faster because of larger exciton oscillator strength in smaller dots.[40,42] As the QD size decreases, the electron wave function penetrates deeper into the barrier and increases the optical matrix element; therefore, relatively faster decay processes are observed from smaller dots, i.e., from SQDF (2.75 ns) compared to that of LQDF (3.37 ns). We also found that the carrier lifetimes of all LQDF are quite long $\geq$3.0 ns, which is useful for an IBSC design. The long carrier radiative lifetime facilitates the photocarrier collection to the IB and improves the efficiency of IBSCs.[13,43] A model calculation reported that a recombination carrier lifetime >3.0 ns could be useful for efficient IBSCs.[12]

Figure 7(a) shows the temperature dependence PL decay curve of LQDF in the 8.0 ML QD structure measured with excitation power at 5.0 mW/cm^2. Here, we present five different temperature decay curves [77 K (red curve), 125 K (green curve), 200 K (blue curve), 225 K (purple curve), and 300 K (pink curve)] fitted with double-exponential decay function (black lines). We found that decay rates are almost the same for the LQDF and SQDF (decay traces for SQDF are not shown here) at 77–125 K, while it decrease significantly for both LQDF and SQDF above 125 K. We also found that the decrease in decay rates is different for LQDF and SQDF above 125 K. Figure 7(b) shows the carrier lifetime of LQDF (circles) and SQDF (triangles) as a function of temperature. It shows that between 77 and 125 K, τ remains almost the same, i.e., ~3.30 ns for LQDF and ~2.75 ns for SQDF. On the other hand, between 150 and 300 K, τ decreases slowly from 2.75 to 1.25 ns for LQDF, while it decreases rapidly from 1.50 to 0.30 ns for SQDF. Usually, the decrease in the carrier lifetime at high sample temperatures is explained due to thermally activated nonradiative channels located at the QD heterostructure interface or in the barrier.[35,38] Here, we hypothesize that at a sufficiently high temperature above 125 K, SQDF experiences a relatively large rate of thermally activated carrier escape back into the WL, leading to a strong reduction of the carrier
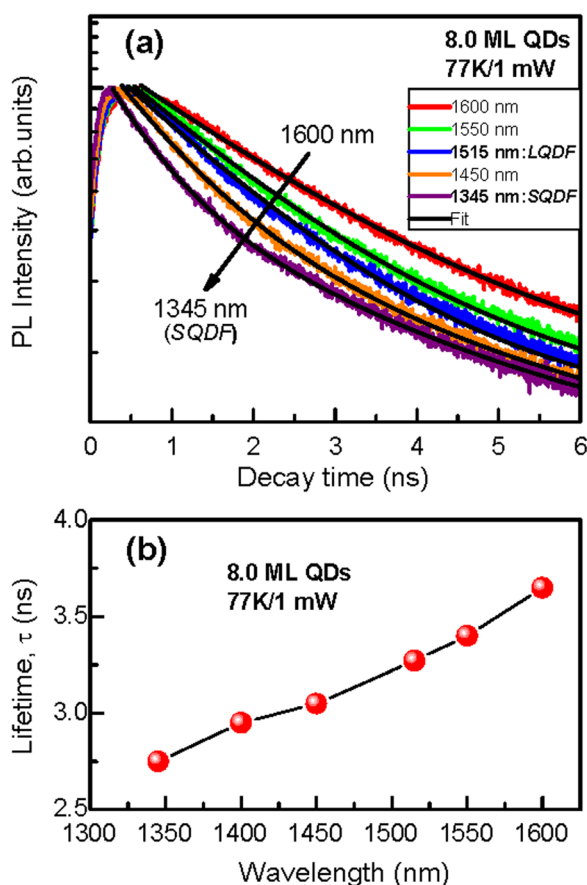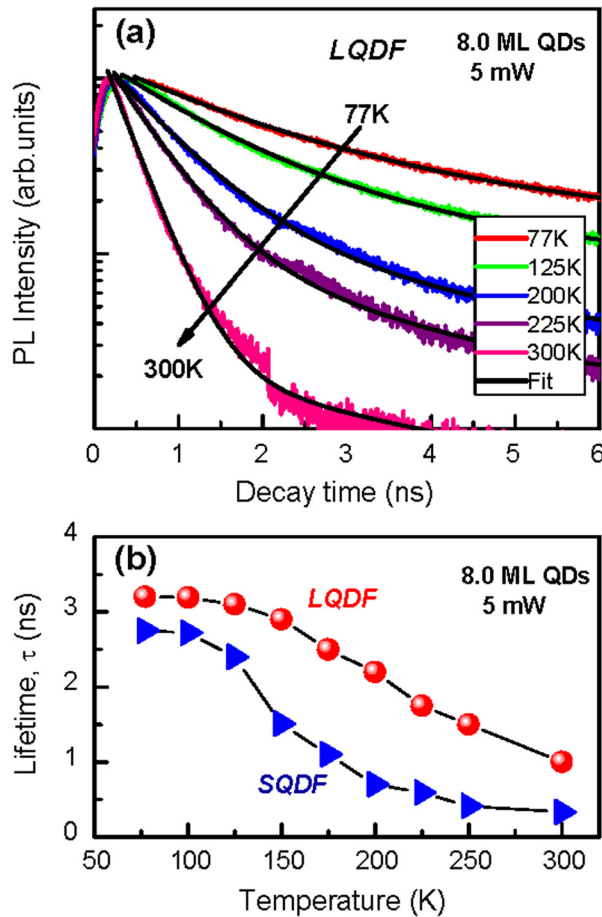
FIG. 7. (a) PL decay curves of LQDF in 8.0 ML QDs with five different temperatures [77 K (red curve), 125 K (green curve), 200 K (blue curve), 225 K (purple curve), and 300 K (pink curve)] measured at 5 mW/cm^2. (b) The comparison of carrier lifetime between LQDF [(red) circles] and SQDF [(blue) triangles] as a function of measured temperature. The solid lines connecting the data points are guides to the eye.

lifetime. In the meantime, carrier recapture from WL causes the population of the LQDF, leading to a slower decrease of carrier lifetime although thermally activated additional non-radiative channels eventually start to cause the decrease of the lifetime at a higher temperature. These TRPL results again confirm the carrier escape and their redistribution between SQDF and LQDF in our InAs/AlAsSb bimodal QD structure. Also, a similar trend of thermally activated carrier lifetime and their escape/transfer mechanism have been reported by a rate equation model in the bimodal InAs/GaAs QD system.[30,35]

IV. CONCLUSIONS

We developed high-quality and reproducible InAs QDs (5.0–8.0 ML nominal thickness) on digital AlAsSb matrix lattice-matched to InP(001) substrates by MBE. The digitally grown AlAsSb matrix provided high crystalline quality with better control of alloy composition. All QDs showed bimodal size distribution and denoted by two QD families of SQDF and LQDF. AFM analysis showed that both SQDF and LQDF have a higher average areal density in 8.0 ML QDs (total density $\sim 9.0 \times 10^{10}$/cm^2) than that of lower thicknesses 5.0–7.0 ML QDs. The dot densities in LQDF are a

little bit higher than those in SQDF in all QD samples presented in this work. The optical properties of bimodal QDs were evaluated by means of excitation power and temperature dependent PL and TRPL measurements. Power dependent PL showed that both SQDF and LQDF have a linear relationship between the PL peak energy and the cube root of the excitation power, which is a signature of type-II transition. Temperature dependent PL showed thermal quenching starts at relatively low temperature ≥ 100 K, which is also a characteristic of type-II QDs. Above 125 K, the continuous increase in the PL intensity ratio between LQDF and SQDF and the anomalous PL peak energy shift of SQDF indicated that carriers have been thermally activated outside of the SQDF into the WL and then relaxed into LQDF. At 77 K, the TRPL measurement showed longer carrier radiative lifetimes of 3.37 ns and 2.75 ns in LQDF and SQDF, respectively. At higher temperatures (150–300 K), the lifetime of SQDF decreased rapidly from 1.50 to 0.30 ns, while it decreased slowly from 2.75 to 1.25 ns in LQDF. This result further confirmed the thermally activated carrier escape and their redistribution between SQDF and LQDF through the WL state.

[1]A. Luque and A. Martí, Phys. Rev. Lett. **78**, 5014 (1997).
[2]W. Shockley and H. J. Queisser, J. Appl. Phys. **32**, 510 (1961).
[3]R. R. King, D. C. Law, K. M. Edmondson, C. M. Fetzer, G. S. Kinsey, H. Yoon, R. A. Sherif, and N. H. Karam, Appl. Phys. Lett. **90**, 183516 (2007).
[4]M. Y. Levy and C. Honsberg, IEEE Trans. Electron Devices **55**, 706 (2008).
[5]K. A. Sablon, J. W. Little, V. Mitin, A. Sergeev, N. Vagidov, and K. Reinhardt, Nano Lett. **11**, 2311 (2011).
[6]T. Li, R. E. Bartolo, and M. Dagenais, Appl. Phys. Lett. **103**, 141113 (2013).
[7]Y. Shoji, K. Akimoto, and Y. Okada, J. Phys. D: Appl. Phys. **46**, 024002 (2013).
[8]R. B. Laghumavarapu, B. L. Liang, Z. S. Bittner, T. S. Navruz, S. M. Hubbard, A. Norman, and D. L. Huffaker, Sol. Energy Mater. Sol. Cells **114**, 165 (2013).
[9]S. Hatch, J. Wu, K. Sablon, P. Lam, M. C. Tang, Q. Jiang, and H. Y. Liu, Opt. Express **22**, A679 (2014).
[10]M. C. Debnath, T. D. Mishima, M. B. Santos, Y. Cheng, V. R. Whiteside, I. R. Sellers, K. Hossain, R. B. Laghumavarapu, B. L. Liang, and D. L. Huffaker, J. Appl. Phys. **119**, 114301 (2016).
[11]Z. S. Bittner, S. Hellstroem, S. J. Polly, R. B. Laghumavarapu, B. Liang, D. L. Huffaker, and S. M. Hubbard, Appl. Phys. Lett. **105**, 253903 (2014).
[12]A. S. Lin, W. Wang, and J. D. Phillips, J. Appl. Phys. **105**, 064512 (2009).
[13]K. Nishikawa, Y. Takeda, K. Yamanaka, T. Motohiro, D. Sato, J. Ota, N. Miyashita, and Y. Okada, J. Appl. Phys. **111**, 044325 (2012).
[14]E. Hall, H. Kroemer, and L. A. Coldren, J. Cryst. Growth **203**, 447 (1999).
[15]Y. H. Zhang, J. Cryst. Growth **150**, 838 (1995).
[16]P. J. Simmonds, R. B. Laghumavarapu, M. Sun, A. Lin, C. J. Reyner, B. Liang, and D. L. Huffaker, Appl. Phys. Lett. **100**, 243108 (2012).
[17]I. A. Karpovich, B. N. Zvonkov, N. V. Baidus, S. V. Tikhov, and D. O. Filatov, *Trends in Nanotechnology Research* (Nova Science, New York, 2004), pp. 173–208.
[18]L. Brusaferri, S. Sanguinetti, E. Grilli, M. Guzzi, A. Bignazzi, F. Bogani, L. Carraresi, M. Colocci, A. Bosacchi, P. Frigeri, and S. Franchi, Appl. Phys. Lett. **69**, 3354 (1996).

[19]K. H. Schmidt, G. Medeiros-Ribeiro, U. Kunze, G. Abstreiter, M. Hagn, and P. M. Petroff, J. Appl. Phys. **84**, 4268 (1998).

[20]H. Kissel, U. Müller, C. Walther, W. T. Masselink, Yu. I. Mazur, G. G. Tarasov, and M. P. Lisitsa, Phys. Rev. B **62**, 7213 (2000).

[21]N. P. Kobayashi, T. R. Ramachandran, P. Chen, and A. Madhukar, Appl. Phys. Lett. **68**, 3299 (1996).

[22]V. A. Shchukin, N. N. Ledentsov, P. S. Kop'ev, and D. Bimberg, Phys. Rev. Lett. **75**, 2968 (1995).

[23]A. L. Barabási, Appl. Phys. Lett. **70**, 2565 (1997).

[24]A. E. Zhukov, V. M. Ustinov, A. R. Kovsh, A. Yu. Egorov, N. A. Maleev, N. N. Ledentsov, A. F. Tsatsulnikov, M. V. Maximov, Yu. G. Musikhin, N. A. Bert, P. S. Kopev, D. Bimberg, and Zh. I. Alferov, Semicond. Sci. Technol. **14**, 575 (1999).

[25]H. Y. Liu, I. R. Sellers, T. J. Badcock, D. J. Mowbray, M. S. Skolnick, K. M. Groom, M. Gutiérrez, M. Hopkinson, J. S. Ng, J. P. R. David, and R. Beanland, Appl. Phys. Lett. **85**, 704 (2004).

[26]T. Baier, U. Mantz, K. Thonke, R. Sauer, F. Schäffler, and H. J. Herzog, Phys. Rev. B **50**, 15191 (1994).

[27]C. Weisbuch and B. Vinter, *Quantum Semiconductor Structures: Fundamentals and Applications* (Elsevier, 1991).

[28]U. E. H. Laheld, F. B. Pedersen, and P. C. Hemmer, Phys. Rev. B **52**, 2697 (1995).

[29]Y. D. Jang, T. J. Badcock, D. J. Mowbray, M. S. Skolnick, J. Park, D. Lee, H. Y. Liu, M. J. Steer, and M. Hopkinson, Appl. Phys. Lett. **92**, 251905 (2008).

[30]G. M. Matutano, I. Suárez, J. C. Ferrer, B. Alén, D. Rivas, L. Seravalli, G. Trevisi, P. Frigeri, and J. M. Pastor, J. Appl. Phys. **111**, 123522 (2012).

[31]J. W. Tomm, T. Elsaesser, Yu. I. Mazur, H. Kissel, G. G. Tarasov, Z. Ya. Zhuchenko, and W. T. Masselink, Phys. Rev. B **67**, 045326 (2003).

[32]X. L. Zhou, Y. H. Chen, T. F. Li, X. L. Ye, B. Xu, and Z. G. Wang, Appl. Phys. Lett. **99**, 031903 (2011).

[33]Y. C. Zhang, C. J. Huang, F. Q. Liu, B. Xu, J. Wu, Y. H. Chen, D. Ding, W. H. Jiang, X. L. Ye, and Z. G. Wang, J. Appl. Phys. **90**, 1973 (2001).

[34]Y. P. Varshni, Physica **34**, 149 (1967).

[35]W. Yang, R. R. L. Webb, H. Lee, and P. C. Sercel, Phys. Rev. B **56**, 13314 (1997).

[36]S. Sanguinetti, D. Colombo, M. Guzzi, E. Grilli, M. Gurioli, L. Seravalli, P. Frigeri, and S. Franchi, Phys. Rev. B **74**, 205302 (2006).

[37]S. Hinooda, S. Loualiche, B. Lambert, N. Bertru, M. Paillard, X. Marie, and T. Amand, Appl. Phys. Lett. **78**, 3052 (2001).

[38]W.-M. Schulz, R. Roßbach, M. Reischle, G. J. Beirne, M. Bommer, M. Jetter, and P. Michler, Phys. Rev. B **79**, 035329 (2009).

[39]F. Hatami, M. Grundmann, N. N. Ledentsov, F. Heinrichsdorff, R. Heitz, J. Böhrer, D. Bimberg, S. S. Ruvimov, P. Werner, V. M. Ustinov, P. S. Kop'ev, and Zh. I. Alferov, Phys. Rev. B **57**, 4635 (1998).

[40]H. Born, L. M. Kirsch, R. Heitz, A. Hoffmann, and D. Bimberg, Phys. Status Solidi B **228**, R4 (2001).

[41]M. Sun, P. J. Simmonds, R. B. Laghumavarapu, A. Lin, C. J. Reyner, B. Liang, and D. L. Huffaker, in *IEEE 39th Photovoltaic Specialists Conference* (2013), p. 3493.

[42]Y. C. Zhang, A. Pancholi, and V. G. Stoleru, Appl. Phys. Lett. **90**, 183104 (2007).

[43]M. Yoshida, N. J. Ekins-Daukes, D. J. Farrell, and C. C. Phillips, Appl. Phys. Lett. **100**, 263902 (2012).